AGU PUBLICATIONS

JGR

Journal of Geophysical Research: Solid Earth

RESEARCH ARTICLE
10.1002/2013JB010785

**Key Points:**
- Depth distribution of seismic anisotropy is inferred from RFs and SKS modeling
- Coherent lithospheric anisotropy calls for a regional scale delamination
- Asthenospheric anisotropy is consistent with the hotspot frame plate motion direction?

**Supporting Information:**
- Readme
- Figure S1

**Correspondence to:**
H. Yuan,
huaiyu.yuan@mq.edu.au

**Citation:**
Yuan, H., and V. Levin (2014), Stratified seismic anisotropy and the lithosphere-asthenosphere boundary beneath eastern North America, *J. Geophys. Res. Solid Earth*, *119*, doi:10.1002/2013JB010785.

Received 22 OCT 2013
Accepted 14 MAR 2014
Accepted article online 18 MAR 2014

# Stratified seismic anisotropy and the lithosphere-asthenosphere boundary beneath eastern North America

**Huaiyu Yuan[1,2,3] and Vadim Levin[4]**

[1]ARC Centre of Excellence for Core to Crust Fluid Systems, Department of Earth and Planetary Sciences, Macquarie University, New South Wales, Australia, [2]Centre for Exploration Targeting, University of Western Australia, Perth, Western Australia, Australia, [3]Geological Survey of Western Australia, Department of Mines and Petroleum, East Perth, Western Australia, Australia, [4]Department of Earth and Planetary Sciences, Rutgers University, Piscataway, New Jersey, USA

**Abstract** Long records of teleseismic observations accumulated at permanent seismic stations Harvard, MA; Palisades, NY; and Standing Stone, PA, in eastern North America are inverted for vertical distribution of anisotropic parameters. High-resolution anisotropy-aware *P* wave receiver function analysis and multiple-layer core-refracted *SKS* waveform modeling favor more than one layer of anisotropy beneath all sites. Our analyses suggest that the depth sensitivity to stratified anisotropic seismic velocity in converted phases and the *SKS* waveforms are complementary and confirm that these two approaches yield consistent lithospheric anisotropic fast axis directions. We illustrate the feasibility of the lithosphere-asthenosphere boundary detection on a regional scale through anisotropy-aware receiver functions. Joint interpretation of receiver functions and *SKS* waveforms beneath eastern North America suggests a thin (~100 km) anisotropic lithosphere with fast axis orientation nearly orthogonal to the strike of major tectonic units and an underlying anisotropic asthenosphere with fast axis directions that favor the HS3-NUVEL 1A plate motion model. Consistent lithospheric anisotropy inferred from both techniques suggests broad presence of coherent fabric in the lower lithosphere, possibly developed in a regional scale delamination event after the assembly of Appalachians.

## 1. Introduction

A link between the deformation of the upper mantle rocks and the directional dependence (anisotropy) of seismic wave speed within them is an essential element of modern structural seismology studies. It provides a means to "see" processes at depth that are suggested by observations of plate motion, by differences in absolute wave speed inferred from tomography, and by scenarios of past tectonic evolution [*Park and Levin*, 2002; *Long and Becker*, 2010]. Observations of seismic anisotropy beneath continents face an interpretational challenge; however, in that, both the lithospheric mantle and the asthenosphere beneath it are made of materials that are likely to become anisotropic under strain [*Ribe*, 1992; *Zhang and Karato*, 1995]. The early debates over where the anisotropy resides, and whether it reflects present or past deformation (illustrated in Figure 1 [*Silver*, 1996]), have been largely settled by the recognition that both volumes of olivine-rich rocks will likely have systematic texture imparted onto them by past tectonic events and/or current plate motion, or both [e.g., *Silver*, 1996; *Vinnik et al.*, 1998; *Fouch and Rondenay*, 2006].

The importance of vertical variations in mantle rock texture was brought to the fore recently by the reinvigorated debate over the depth to, and nature of, the lithosphere-asthenosphere boundary (LAB). The boundary, which has to exist for plate tectonic framework to hold, has been singularly difficult to pin down [*Eaton et al.*, 2009; *Fischer et al.*, 2010]. A distinction to be drawn here is between the *thickness* of the lithosphere and the actual *boundary* separating it from the upper mantle that is free to flow. While the former may be inferred from a variety of observations (e.g., long wavelength seismic tomography, observations of gravity and geoid shape, chemical composition of xenoliths, and heat flow), detection and characterization of the latter is the outstanding "grand" challenge for seismologists [*Lay,* 2009]. A big part of the LAB detection challenge lies in disparities in sensitivity, e.g., between surface wave analysis and long-range refraction profiles, or between local (receiver functions) and path-averaged (seismic tomography) probes. The degree of illumination of the target depth region (100 to 300 km) by combinations of observing seismic stations and opportunely placed earthquakes (or sometimes explosions) is also greatly uneven over the Earth's surface.

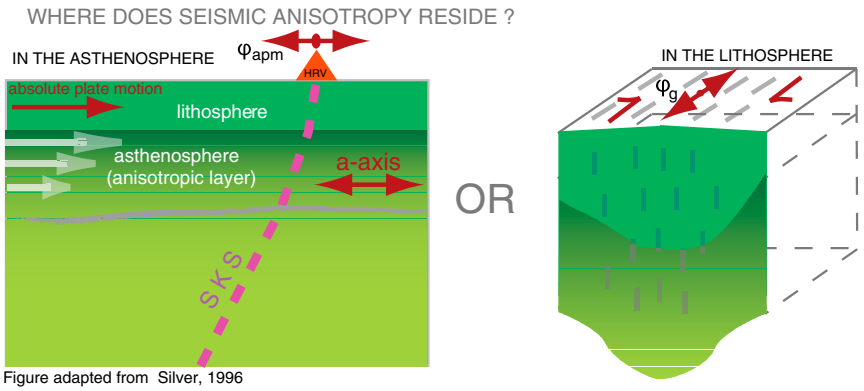


**Figure 1.** Vertical variation of anisotropy in the shallow upper mantle. If anisotropic properties are restricted to a single layer (either frozen into the lithosphere or formed in the asthenosphere by current mantle flow), we can use the observed polarization of split shear waves as a representation of the past deformation (in the lithosphere) or current deformation (in the asthenosphere). The $\varphi_{apm}$ and $\varphi_g$ represent the apparent fast axis directions inferred from *SKS*.

In North America, a number of studies have already employed USArray data together with other seismological resources in order to delineate the LAB, primarily by means of timing the mode-converted waves (either from *P* to *S* or from *S* to *P*) that likely arise from it [*Abt et al.*, 2010; *Levander et al.*, 2011; *Kumar et al.*, 2012]. Similar mapping of the LAB has also been attempted on a global scale by *Rychert and Shearer* [2009]. It is noteworthy that one of the main outcomes of these studies has been a paradox. In most places, where data permitted, an abrupt impedance contrast consistent with a decrease of speed with depth has been detected, between 80 and 130 km, by both *P*-to-*S* and *S*-to-*P* conversions. This depth range is a natural position to look for the LAB beneath young continental areas and most oceanic plates. For the majority of the stable continents, however, this is not deep enough: down to ~200 km, or deeper continental lithosphere is suggested by tomographic and heat flow studies [e.g., *Gung et al.*, 2003; *Artemieva*, 2009] and thermobarometric analysis of xenoliths from lithospheric mantle [e.g., *O'Reilly and Griffin*, 2010]. Contributing to the "challenge" of the LAB detection is the apparent similarity of the signature of an "LAB" feature from the areas of thick and thin lithosphere, seen in the studies of the North American continent [*Abt et al.*, 2010; *Kumar et al.*, 2012] as well as Australia [*Ford et al.*, 2010]. In essence, the same observation requires different explanations depending on the geography [*Abt et al.*, 2010; *Kumar et al.*, 2012].

To solve this conundrum, a concept of a "mid-lithospheric discontinuity" (MLD) has been put forth [e.g., *Fischer et al.*, 2010]. The MLD is proposed as a global feature [*Romanowicz*, 2009], which had been consistently found in early long-range profiling studies [*Thybo and Perchuc*, 1997]. The nature of the MLD remains unknown and may be associated with, e.g., accumulated melts [*Thybo*, 2006; *Kawakatsu et al.*, 2009; *Sleep*, 2009], sharp drop of water storage capacity of hydrous mineral [*Mierdel et al.*, 2007; *Green et al.*, 2010], remnants of fossil subduction interfaces [*Bostock*, 1998; *Jones et al.*, 2003; *Chen et al.*, 2009], a peak in shear wave attenuation due to elastically accommodated grain boundary sliding [*Karato*, 2012], a change of upper mantle rock texture [*Levin and Park*, 2000; *Yuan and Romanowicz*, 2010], or relict deformation structures produced during the formation of the cratonic lithosphere [*Cooper and Miller*, 2014]. In this view, the LAB coincides with the MLD beneath areas of recent tectonic activity and departs from it downward in stable platforms and cratons. Because the MLD corresponds to a sharp negative gradient in seismic impedance with depth, material in the lower part of the stable continental lithosphere (that is, below the MLD) needs to be notably slower, at least locally. On the other hand, the transition from that material into asthenosphere at depths of 200–250 km [*Eaton et al.*, 2009; *Fischer et al.*, 2010] has to be gradual enough not to cause conversions in either *P* or *S* waves.

A recently developed 3-D model of shear wave velocity and anisotropy beneath the North American continent [*Yuan et al.*, 2011] addresses the long-standing argument regarding the provenance of seismic anisotropy, with directional dependency of wave speed placed in both the lithosphere and the asthenosphere. Figure 2 shows the averaged 1-D velocity structure profiles of two representative regions in central and eastern North America. In the Superior cratonic region, the model of *Yuan et al.* [2011] shows high velocity peaking at a depth of 150 km and smoothly decreasing downward to depths over 300 km. On the other hand, the azimuthal anisotropy displays more variation with depth: multiple local peaks in strength are

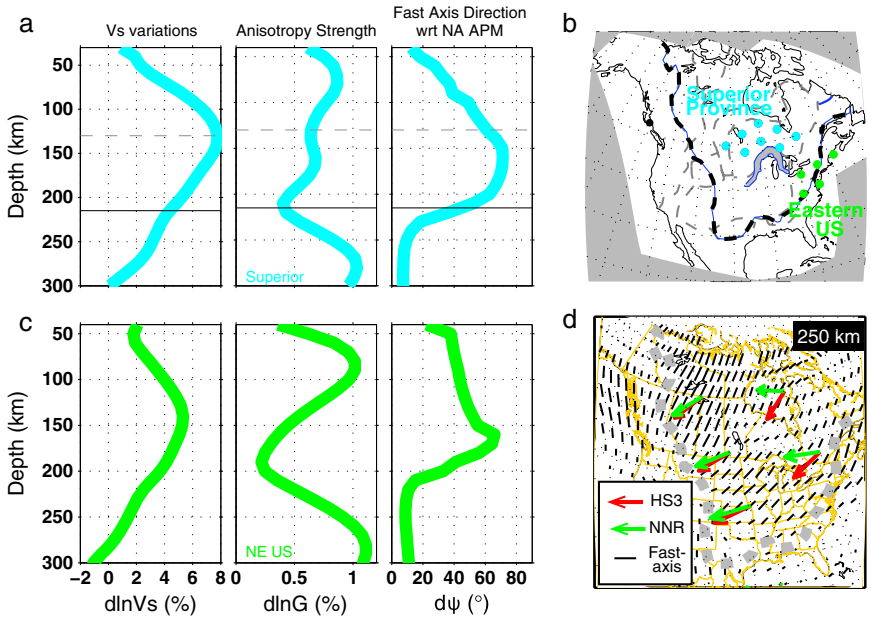


**Figure 2.** Shear wave velocity depth profiles for selected regions in North American from *Yuan et al.*'s [2011] model: (a) Superior region. (a1) shear wave variation, (a2) azimuthal anisotropy strength, and (a3) fast axis direction with respect to the absolute plate motion direction in the HS3-NUVEL 1A model [*Gripp and Gordon,* 2002]. (b) Sample location for the selected regions. (c) Same as Figure 2a but for the northeastern U.S. region. (d) APM directions and anisotropy direction at 250 km from *Yuan et al.*'s [2011] model. Red arrow, HS3-NUVEL 1A and green arrow, NNR-NUVEL 1A. Black sticks show the anisotropy direction. Note the departure of the NNR mode from anisotropy observations in eastern North America.

observed, which are associated with distinct fast axis directions indicating the presence of several domains of anisotropy. Below 200 km, an abrupt change in fast axis direction toward the absolute plate motion (APM; Figure 2d) is evident, while above the fast axis direction is at a high angle to the APM. *Yuan and Romanowicz* [2010] suggest that the deep APM parallel domain exhibits current deformation in the asthenosphere, while the two shallow domains reflect frozen-in anisotropy in the lithosphere. The respective vertical boundaries of anisotropy correlate with proposed depths of the mid-lithospheric discontinuity (horizontal dashed line in Figure 2a) and the LAB (horizontal solid line in Figure 2a). *Yuan and Romanowicz* [2010] argue that the top of the lower horizon marks an anisotropic LAB, which overlies the asthenosphere with a uniform absolute plate motion parallel fast axis direction, and the shallow horizon delimits an ancient chemically depleted and rheologically strong upper layer [*Griffin et al.*, 2004; *Cooper et al.*, 2004].

However, due to its continent-wide coverage, *Yuan et al.*'s [2011] model has lateral resolution on the scale of 500 km and is expected to average and, thus possibly misrepresent, the structure in regions with abrupt lateral changes in properties. One such region is the New England Appalachians. One of the earliest cases for stratified anisotropy was built on data from this part of North America [*Levin et al.*, 1999]. Global models of seismic velocity show thick (~150 km) lithosphere extending to the eastern coast of North American continent, while regional and local studies with better lateral resolution [e.g., *Van der Lee*, 2002; *Li et al.*, 2003] suggest that a region of thinner lithosphere (~100 km) exists along the coast. This view is also supported by studies using body wave conversions [*Rychert et al.,* 2005, 2007; *Abt et al.*, 2010]. Interestingly, the variation in speed is not gradual from the center of the continent to the edge. Rather, significant lateral variations on different scales exist along the coastline [*Menke and Levin*, 2002; *Van der Lee*, 2002; *Nettles and Dziewonski*, 2008]. Offshore modeled high velocity variations in the Atlantic indicate oceanic lithosphere over 100 km thick [*Grand and Helmberger*, 1984; *Yuan et al.*, 2014]. Figure 2c illustrates the averaged surface wave velocity profiles in the region that suggest a fairly thick (>150 km) domain of anisotropy in the uppermost mantle, a region where azimuthal anisotropy is relatively weak (150–220 km), and a lower domain where anisotropy is stronger. Due to the broad lateral averaging in the model, it is likely that lateral variations are smoothed out within 500 km distance range that spans from the eastern corner of craton to the orogenic deformation zones of Grenville and Appalachians and the old Atlantic oceanic lithosphere (e.g., see Figure 3).

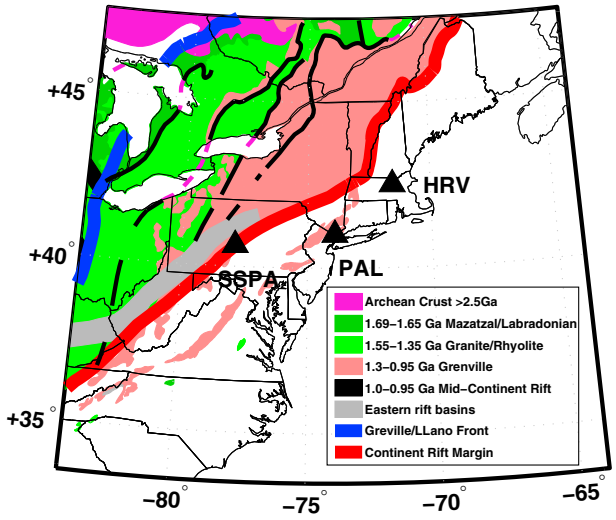


**Figure 3.** Regional tectonic setting modified from *Whitmeyer and Karlstrom* [2007] and station location. Thick blue and red lines are for the Grenville deformation front and the Laurentia continent rift margin. The latter delimits the cratonic region from thin lithosphere in the Appalachians in regional tomographic images [e.g., *Yuan et al.*, 2011].

In this paper we develop high-quality constraints on the vertical and lateral variation in attributes of anisotropy at three locations in the region, which we then compare (and contrast) with structure predicted for this region by the *Yuan et al.*'s [2011] model. We use a combination of two complementary techniques, an anisotropy-aware receiver function analysis [*Levin and Park*, 2000] and an inversion for multiple layers of anisotropy on the basis of directionally variable shear wave splitting [*Yuan et al.*, 2008]. Compared with the regional surface wave model, these two methods are capable of resolving anisotropic structure beneath a single seismic station. The combination of these two techniques is complementary because *P-S* mode conversion is primarily sensitive to vertical gradients in properties [*Levin and Park*, 1997], while birefringence in *SKS* (and similar) phases is an integral measure of anisotropic properties along their near-vertical paths (Figure 4). Our data come from one of the longest operating broadband stations, HRV (Harvard, MA), which provides over 2 decades of *SKS* observations and 2 decades of *P* waves from large earthquakes ($M_w >= 6.0$) for receiver functions. We also use data from similarly long-running nearby observatories (PAL, Palisades, NY and SSPA, Standing Stone, PA). Figure 3 shows the station locations with respect to the major tectonic structures of the region. This study represents a return, of sorts, to the region previously investigated by *Levin et al.* [1999]. Since that initial study, vastly more data have accumulated, and these data facilitate a new look at the seismic anisotropy parameters of the upper mantle.

## 2. Abrupt Changes in Upper Mantle Rock Fabric: Evidence From *P-S* Converted Waves

At HRV, we use 211 *P* wave records from large ($M_w$6.0 and over) earthquakes within 90° from the station in the time interval 1990–2006. A 16 year long observation period captures the distribution of the global seismicity well and makes it possible to limit the data to most clear records, primarily from the Pacific subduction zones (Figure 5). Focus on the larger events is advantageous for the goals of resolving boundaries such as LAB that are potentially smooth and visible only in longer periods. We choose direct *P* wave data on the basis of signal strength with respect to the microseism level and use visual inspection to screen for interferences from cultural noise, transmission problems, and occasional overlaps with phases from other earthquakes. From selected records, we construct direction- and epicentral-dependent receiver function (RF) gathers using the multitaper spectral correlation tool of *Park and Levin* [2000]. In horizontally stratified isotropic medium, *P*-to-*S* converted phases should be similar for all the directions of wave propagation. Directional dependence of observed conversions is diagnostic of either the dip of the converting impedance contrast or the presence of anisotropy next to it, or both [*Bostock*, 1997; *Levin and Park*, 1997]. The region we choose for study is well illuminated by earthquakes from azimuthally distributed source regions (Figure 5).

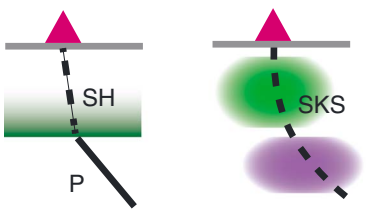


**Figure 4.** Depth sensitivity illustrated for (left) receiver function analysis and (right) *SKS* modeling. Dashed lines indicated the shear wave (*P-SH* and *SKS*) paths. Preferred anisotropy depth distribution (shaded) is inferred from this study. See Discussion for details.

Results are presented in Figure 6 for two most data-rich quadrants (NW and SE) that yield patterns with many similar features, but also some significant variation. Our analysis for *P-SV* conversions (shown on radial components of receiver functions) is very similar to that previously carried out by *Rychert et al.* [2005, 2007] and especially by *Rychert and Shearer* [2009]. We find three

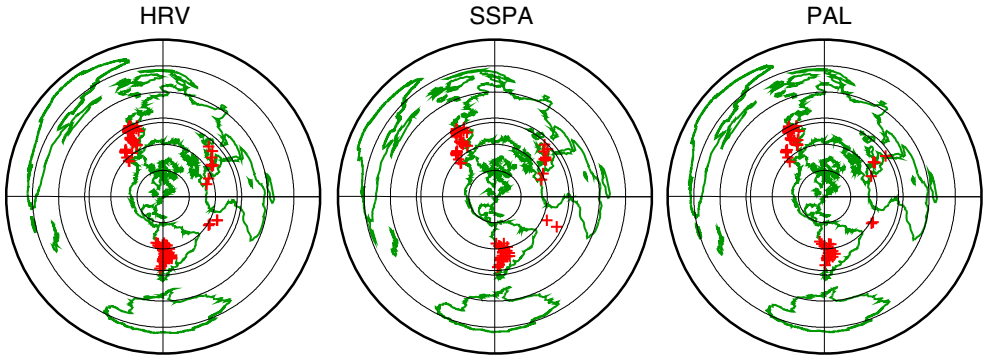


**Figure 5.** Event distributions for receiver function analysis. Stations are in the center of the plot; red crosses show the events. Distance from the station is marked in 30° increments; 90° distance limit for direct *P* wave observation is marked by a double circle.

main phases that have attributes such as directional stability, and a proper moveout with changing ray parameter, that are consistent with subhorizontal converting boundaries at depth. As previously discussed by *Rychert et al.* [2007], these phases likely mark the crust-mantle transition (positive pulse at ~3.5–4 s), the MLD (negative pulse at 6.5 s), and the LAB (rather small negative pulse at 10–11 s, nearly overprinted with the strong crustal multiple at 12 s). Notably, from the SE, the LAB pulse seems to arrive at systematically later times. In Figure S1 in the supporting information, we show an epicentral gather of all the RFs in our data set for HRV with predictions of arrival times of converted waves from the Moho, the crustal multiples, and the likely LAB boundary. Phases in the 12–15 s time delay range display a characteristic moveout of the multiple reflected *P-S* converted wave from the Moho.

We compare the timing of *P-SV* converted phases to *P-SH* energy seen on the transverse component, which has not been studied before. We note very systematic features. A sequence of polarity-reversed pulses (negative from NW and positive from SE) appears in the 2–4 s time window, synchronous with or earlier than the crust-mantle phase on the radial. A very prominent polarity-reversed phase is nearly synchronous with the MLD phase, and similarly large polarity-reversed phase is seen in the 10–12 s time window, the locus of arrivals from the LAB. *P-SH* conversions do not suffer from crustal multiples to the extent that *P-SV* RFs do [*Levin and Park*, 1997], so we can assume that the phases seen after ~5 s arise from *P*-to-*S* conversions within (or below) the lithosphere. Systematic changes in the polarity of *P-SH* conversions can diagnose both the inclination of the converting interface [*Langston*, 1977] and the anisotropic velocity adjacent to the interface [*Bostock*, 1997; *Levin and Park*, 1997]. As *Levin and Park* [1998] discuss in considerable detail, a good test for the latter interpretation is the lack of significant direction-dependent time moveout in such phases, which is what we observe at HRV.

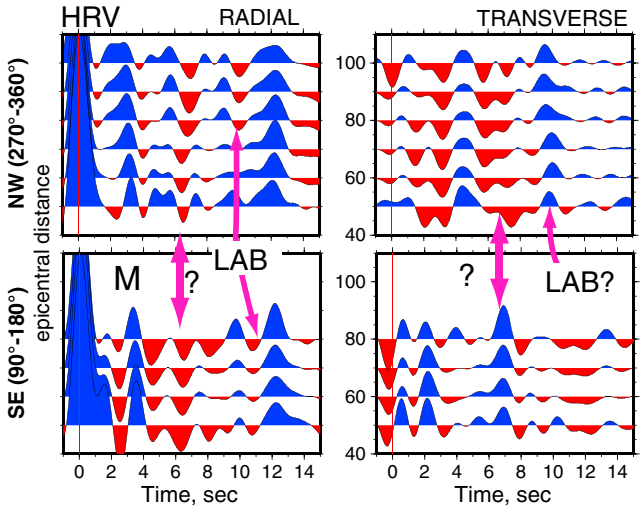


**Figure 6.** (top and bottom) *P* wave receiver function gathers from two back-azimuth directions. Prominent phases are seen in both (left) radial and (right) transverse gathers. Transverse components are amplified. Following *Rychert et al.* [2007], on the radial component, we mark the crust-mantle boundary (M), bottom of the lithosphere (LAB), and a "mid-lithospheric" discontinuity (labeled "?"). The timing of these phases is proportional to the depth of the impedance contrast where they originated. A large positive pulse at ~12 s on the radial is likely a crustal multiple. Prominent phases on the transverse component suggest that anisotropic velocity is likely associated with all the three features (or else they have significant dip from horizontal).

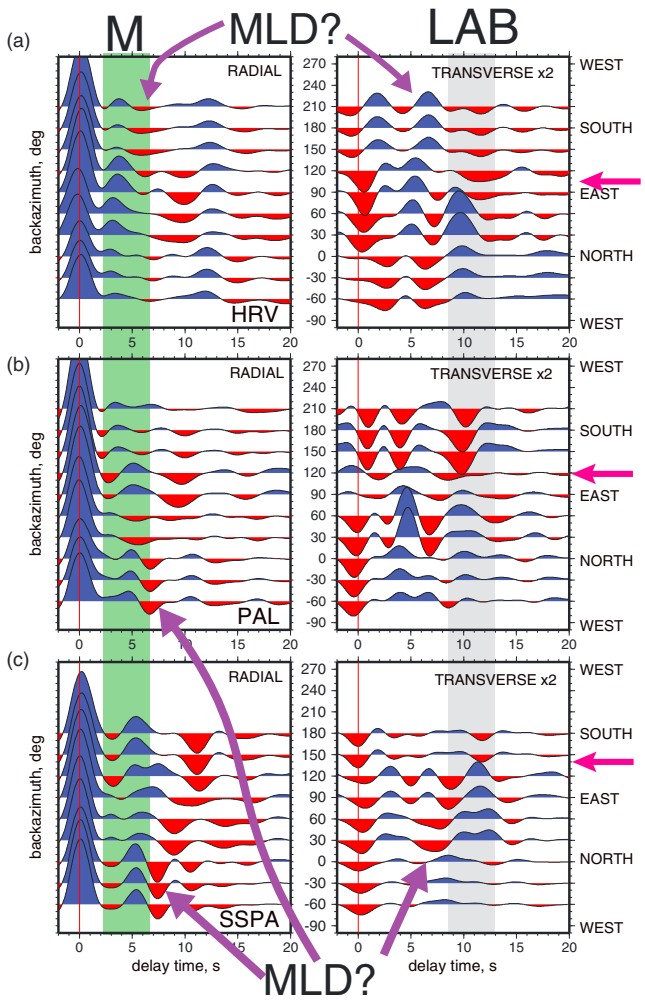


**Figure 7.** Back-azimuth gathers of *P*-to-*S* receiver functions at the three sites in northeastern North America. Transverse components are amplified. Light gray region encloses phases on transverse components likely associated with the LAB. Receiver functions are averaged in 30° wide back-azimuthal bins with 50% overlap and plotted at the central back-azimuth value for the corresponding bins. Frequency content is limited to ~0.25 Hz. Back-azimuth gathers are arranged from south through east to north and exclude the western segment where no sources are present. The systematic polarity changes seen in these phases most likely arise through *P*-to-*S* conversion in the presence of anisotropy [*Levin and Park*, 1997], with anisotropic symmetry axes being aligned with the direction of the polarity flip. Two significant aspects of these patterns are (a) the similarity in timing, which implies relatively uniform LAB depth, and (b) the similarity in the direction of polarity flips, which implies uniform rock fabric beneath the entire region.

Having chosen anisotropy as a preferred interpretation, we can examine the directional pattern of the *P-SH* converted energy, infer likely orientations of the anisotropic symmetry axes at depth [*Levin and Park*, 1998], and then use timing of the pulses to assess the actual depth, where boundaries associated with this anisotropy are. With very large directionally distributed data sets [*Park and Levin*, 2000; *Park et al.*, 2004; *Nikulin et al.*, 2009], it is also possible to diagnose the actual nature of anisotropy (e.g., whether the symmetry axis is slow or fast, and how it is oriented). However, our target phases (*P-S* conversions from MLD and LAB) are within the subcontinental mantle, and an assumption of fast symmetry axis due to olivine lattice preferred orientation [*Ribe*, 1992] is a good initial guess. Figure 7a presents HRV data in the form of a back-azimuth gather. Radial component conversions from the crust-mantle boundary and the MLD are clear, as are the crustal multiples at ~12 s delay, while tracing the LAB is problematic. On the transverse component, however, very clear phases mark all the three boundaries. The polarity switch is especially well established for the LAB phase and takes place at back azimuth 100–110°SE. A clear polarity switch in *P-SH* converted phase implies a symmetry axis in the direction about which the switch occurs. The fact that only one polarity change is seen suggests that the axis is inclined from the vertical [*Levin and Park*, 1998].

Figure 7 shows back-azimuthal RF patterns for HRV and two other long-running seismic sites, PAL and SSPA, in the same region (see Figure 3). Data selection and processing for PAL (125 events) and SSPA (159 events) are similar to HRV. All three sites have RF patterns that display prominent polarity-reversed phases on the transverse component. Arrival times of these phases are consistent with expected converted waves from the LAB. All three sites were examined in previous studies [*Rychert et al.*, 2007; *Abt et al.*, 2010], which report LAB depths on the order of 100 km for them. The direction about which the *P-SH* converted phases reverse is ~120°SE at PAL and ~140°SE at SSPA. Together with HRV, these sites sample a region of ~500 km across, which is approximately the resolution scale of the *Yuan et al.*'s [2011] model for the North American upper mantle anisotropy. Within this region, rock texture that causes anisotropy at the (proposed) LAB boundary appears to be nearly uniform.

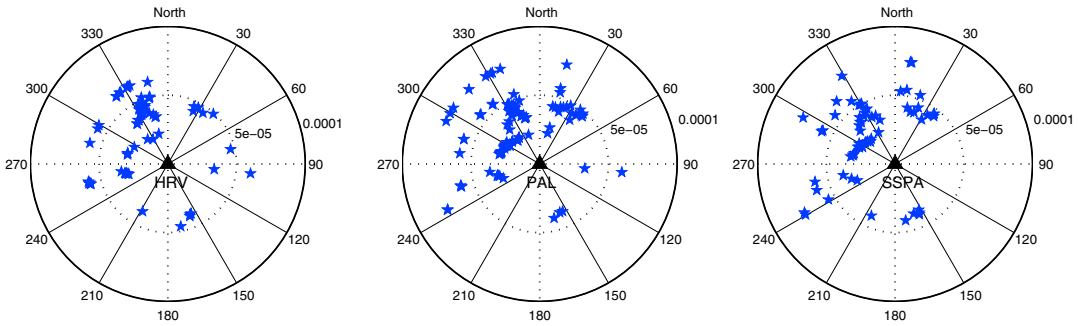


**Figure 8.** *SKS* event distribution plotted in slowness-back-azimuth space. Radial direction shows slowness (s/m). North is indicated.

## 3. Vertical Layering of Anisotropic Properties: Evidence From Split Shear Waves

We use an *SKS* full waveform cross-convolution technique [*Menke and Levin*, 2003; *Yuan et al.*, 2008] to perform inversions for layered anisotropic structures. We closely follow inversion procedures described by *Yuan et al.* [2008]; however, there are significant differences in data processing and error estimation for long-operating permanent stations used in the current study. Below we present a brief introduction of the cross-convolution method and focus on key processing steps in the *SKS* waveform modeling for permanent sites and the associated results.

For a given observation of an *SKS* phase in ray-based coordinates, the horizontal components radial (*R*) and transverse (*T*) contain the *SV*-polarized *SKS* phase and, in case of anisotropic media, an *SH*-polarized phase arising through birefringence (splitting). We can attempt to predict the effect of anisotropy by choosing the parameters of anisotropy and predicting synthetic seismograms with corresponding components *r* and *t*. If the model used to predict the synthetics is close to the real Earth, the cross-convolved terms between the data and the synthetics, *R*t* and *T*r*, where * stands for convolution, should be approximately equal [*Menke and Levin*, 2003]. Because the unknown source term would appear in both pairs of cross-convolved time series, equating *R*t* and *T*r* eliminates the need for a real source time function in the synthetics. In practice, synthetics with a simple *SV* input pulse (e.g., using a ray theoretic approach [*Frederiksen and Bostock*, 2000]) can be efficiently computed.

This cross-convolution technique was used for *SKS* splitting by *Levin et al.* [2006, 2008, 2012] at a number of individual sites and small arrays and was recently applied to receiver function modeling [*Bodin et al.*, 2014]. *Yuan et al.* [2008] further developed the *SKS* method by including an efficient parameter search technique, the Neighborhood Algorithm sampling [*Sambridge,* 1999a], and applied it to a 30-station Billings array in northeast Montana, where small surface aperture (150 km × 120 km) of the deployment enabled robust splitting, waveform modeling, and error estimates through stacking of 30 broadband stations to boost signal-to-noise ratio. The data error was approximated by the standard deviation in the waveform stacking and was propagated using the model appraisal tool in the Neighborhood Algorithm [*Sambridge*, 1999b] to form model errors. In *Yuan et al.* [2008], direct *S* waveforms from several deep events were also used, which were essential for augmenting event azimuthal coverage. Due to the trade-off between anisotropy strength and layer thickness, a fixed 100 km layer thickness was used in the modeling, and only anisotropy strength and fast axis direction were allowed to vary.

Compared with *Yuan et al.* [2008], there are several major differences in modeling permanent station waveforms. First, over 20 years of recordings at these stations warrant a suitable event distribution for studying azimuthal signal in *SKS* waveforms. Figure 8 shows that events used in this study cover nearly two back-azimuthal quadrants, with a few events from the other directions. Long operating times exacerbate the unbalanced distribution of data. Over time areas with high rate of seismicity (e.g., northwestern Pacific and Tonga) contribute progressively larger fraction of the total data set. We thus offset the impact of the intense seismicity regions by applying an arbitrary 30° smoothing window to weight each back-azimuth bin equally (Figure 8).

Error estimation in the current study is through a simple bootstrapping technique [*Efron and Tibshitani*, 1986], given that all permanent sites have a very large number of high signal-to-noise ratio *SKS*/*SKKS* waveforms.

**Table 1.** One-Layer Starting Models[a]

| Thickness (km) | Density (g/cm$^3$) | *Vp* (km/s) | *Vs* (km/s) | Anisotropy Strength (%) | Fast Axis Direction (deg) |
|---|---|---|---|---|---|
| 35 | 2.5 | 6.4 | 3.6 | - | - |
| 100 | 3.1 | 8.0 | 4.6 | (0–20) | (0–180) |
| Half space | 3.3 | 8.2 | 4.7 | - | - |

[a]Anisotropy strength scales peak-to-peak variations to *Vp* and *Vs*. Fast axis direction is clockwise from north. Brackets indicate the bounds allowed for parameter search.

A randomly chosen subset of the data is replaced with duplicates of other waveforms and is used as a data collection for the parameter search. For each station, we generated 200 such data collections. For bootstrapped data set, the space of model parameters (values of anisotropy strength and orientations of fast direction) is explored with a direct Monte Carlo search approach using the Neighborhood Algorithm [*Sambridge*, 1999a; *Yuan et al.*, 2008]. Each of these 200 searches yields a "best" model chosen on the basis of *R*t* and *r*T* misfit. The distribution of all the 200 best models is then used to approximate the model errors by estimating the 1 sigma region of probability density function of the model parameters.

In the current approach, the *SKS* waveform selection is through an automated process. *SKS*/*SKKS* waveforms are first downloaded for all available global events with $M_w > 6.4$ and distance range between 85° and 140°, for the duration of operation of the stations, and then culled based on waveform similarity in the cross-convolved components between data and synthetics. We use a ray theoretical synthetic code [*Frederikson and Bostock*, 1999] to compute synthetic response of a single anisotropic layer with apparent splitting times and fast axis directions inferred from literature (e.g., 1 s and ~90°E fast axis direction for HRV [*Barruol et al.*, 1997; *Levin et al.*, 1999; *Fouch et al.*, 2000; *Liu,* 2009]). We cross-convolve synthetics and data and compute misfits in *L*-2 norm. We treat misfits greater than 2 sigma as outliers and remove the associated waveforms from the data set. We also remove events that are within ±5° of the single-layer apparent fast axis direction, where the splitting-related energy on the transverse component is small and often buried in the noise. The final numbers of available events are 71, 107, and 69 for the three sites (Figure 8). We then bootstrap the final waveforms to form 200 "new" data sets for each station, divide them into back-azimuthal 30° bins (with 10° overlapping), and assign equal weight to each bin. We conduct a global search using the Neighborhood Algorithm for the best models for one-layer anisotropy with horizontal fast axis symmetry axis and for models with two layers of anisotropy with symmetry axes that can be either horizontal or dipping (Tables 1 and 2).

The modeling results are presented in Figures 9–11. In the case of a single layer, Figure 9 plots the normalized probability density functions for the anisotropic parameters from the 200 bootstrap models. We interpret the best model at the maximum probability and indicate the model error bounds by 68% probability region. For station HRV, the modeling results are as follows: the peak of the fast axis direction distribution is approximately east-west (89°E) and that of the splitting time is 0.9 s. The distribution of delay values is quite broad, with 68% region extending from 0.57 to 1.04 s. Fast directions within the 68% probability region are between 80° and 110°. A small secondary mode of the model population is observed for HRV, with a peak of fast axis direction distribution at ~130°. Best models for stations PAL and SSPA are more tightly clustered. The fast axis directions are similar to HRV (N88°E and N87°E), but the splitting times are smaller, especially for station SSPA, where it is under 0.5 s. For comparison, the apparent splitting measurements used by *Yuan et al.* [2011] are HRV, 116.1°SE and 0.9 s; PAL, 85°NE and 1.3 s; and SSPA, 70°NE and 1.2 s [*Liu,* 2009].

Two-layer modeling results from station HRV are shown in Figure 10. The top and bottom layer fast axis directions are 123°SE and 50°NE, and plunges of fast axes are 13° and 34° from the horizontal, accordingly. These results are

**Table 2.** Two-Layer Starting Models[a]

| Thickness (km) | Density (g/cm$^3$) | *Vp* (km/s) | *Vs* (km/s) | Anisotropy Strength (%) | Fast Axis Direction (deg) | Fast Axis Plunge (deg) |
|---|---|---|---|---|---|---|
| 35 | 2.5 | 6.4 | 3.6 | - | - | - |
| 100 | 3.1 | 8.0 | 4.6 | (0–20) | (0–180) | (0–45) |
| 100 | 3.3 | 8.2 | 4.7 | (0–20) | (0–180) | (0–45) |
| Half space | 3.3 | 8.2 | 4.7 | - | - | - |

[a]Same as Table 1 but for two layer models. Fast axis plunge is away from horizontal positive downwards.

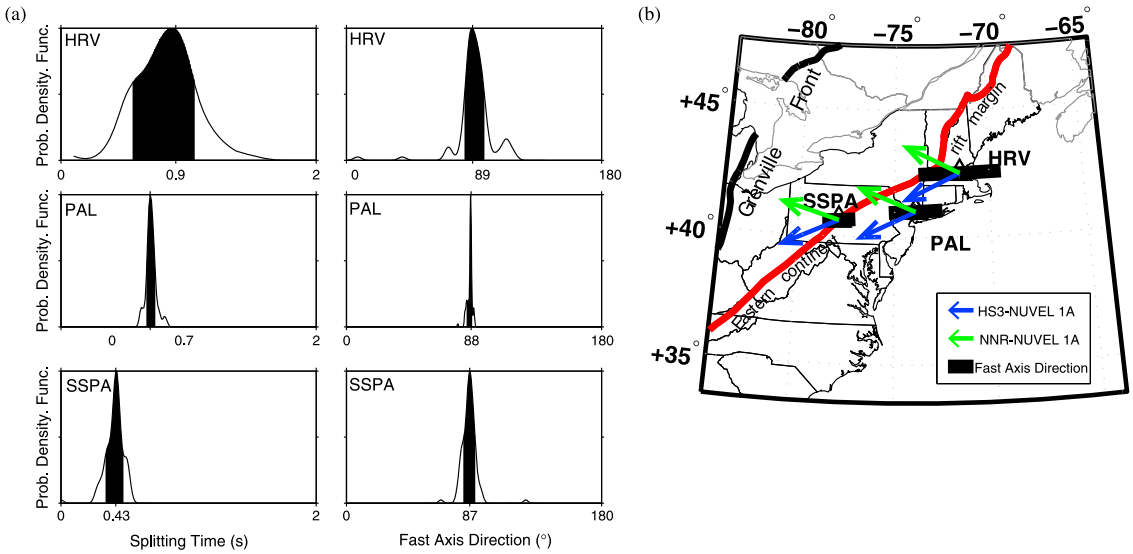


**Figure 9.** (a) One-layer *SKS* modeling results: Plotted are the probability density functions for (left column) anisotropy strength and (right column) fast axis direction of the 200 best models from bootstrapping. The best model and the 1 sigma error bounds are indicated by the *x* axis tick mark and the black shaded region, respectively. (b) Map view showing the regional tectonic trends (Grenville deformation front and the east continent rift margin), single-layer apparent splitting modeling results (splitting time scaled to Figure 9a), and the APM directions from the hotspot frame and no-net rotation frame models.

generally consistent with *Levin et al.* [1999]: 100°SE and 50°NE for the fast axes in the two layers, with 15° and 45° plunge, respectively. The modeled splitting times are slightly larger in this study: 0.8 s and 1.0 s for the top and bottom layers, compared with ~0.7 and 0.9 in *Levin et al.* [1999]. The error bounds in this study are much wider, e.g., over 1.5 s peak-to-peak in splitting times, ~40° in horizontal fast axis directions and 20°–30° in the fast axis plunge. It is however a robust feature that the fast axis directions in the anisotropic layers are significantly distinct. In the top layer, the fast axis is oriented approximately NWW, and in the bottom layer, it is ~NE. The modeling results at stations PAL and SSPA are consistent with HRV (Figure 11): i.e., ~1 s splitting times and NNW and NE-SW anisotropy fast axis directions in the top and the bottom layers, respectively.

## 4. Significance of *SKS* Models

The near east-west fast axis directions obtained from the one-layer modeling of *SKS* data at HRV and PAL are, in general, consistent with those reported by earlier studies in the region [e.g., *Barruol et al.*, 1997; *Levin et al.*, 1999; *Fouch et al.*, 2000; *Liu,* 2009]. Published results for site SSPA by *Barruol et al.* [1997] and *Liu* [2009] show considerable scatter of values, which is neverthness an indication of the presence of multiple and/or dipping anisotropic domains. It is interesting to observe that the dominant east-west fast axis direction does not agree with the absolute plate motion directions (Figure 9) in either the hotspot reference or the no-net rotation frame models (~70°NE for all the three stations in HS3 NUVEL-1A and >100°SE in NNR NUVEL-1A, respectively [*Gripp and Gordon*, 2002; *DeMets et al.*, 1994]), suggesting that the apparent single-layer anisotropy parameters cannot be explained by the flow in the asthenosphere.

Our two-layer modeling results (Figures 10 and 11) agree well with the two-layer models developed earlier by *Levin et al.* [1999, 2000]. A plate-motion-parallel fast axis direction is found in the bottom layer and a NWW-SEE direction in the top layer. The overall regional consistency in the observations at all the three sites favors the interpretation that the bottom layer represents the asthenospheric component of the signal and the top layer represents the anisotropic structure "frozen" within the lithosphere. Compared to the one-layer models, these two-layer models provide a statistically better fit to the data (Table 3): e.g., in all cases, the best two-layer models allowing plunging fast axis direction are statistically superior at over 99% significance level with respect to the one-layer models.

Probability functions developed for individual parameters of the models are fairly narrow for sites PAL and SSPA, while at HRV, they are much broader. Possible causes of this may be structure complexity, or, more likely, noise in the data. Inversion results for site SSPA present an interesting case of anisotropy getting stronger when more layers are introduced into the model: a single-layer model has a cumulative delay of ~0.5 s, while in the two-layer model,

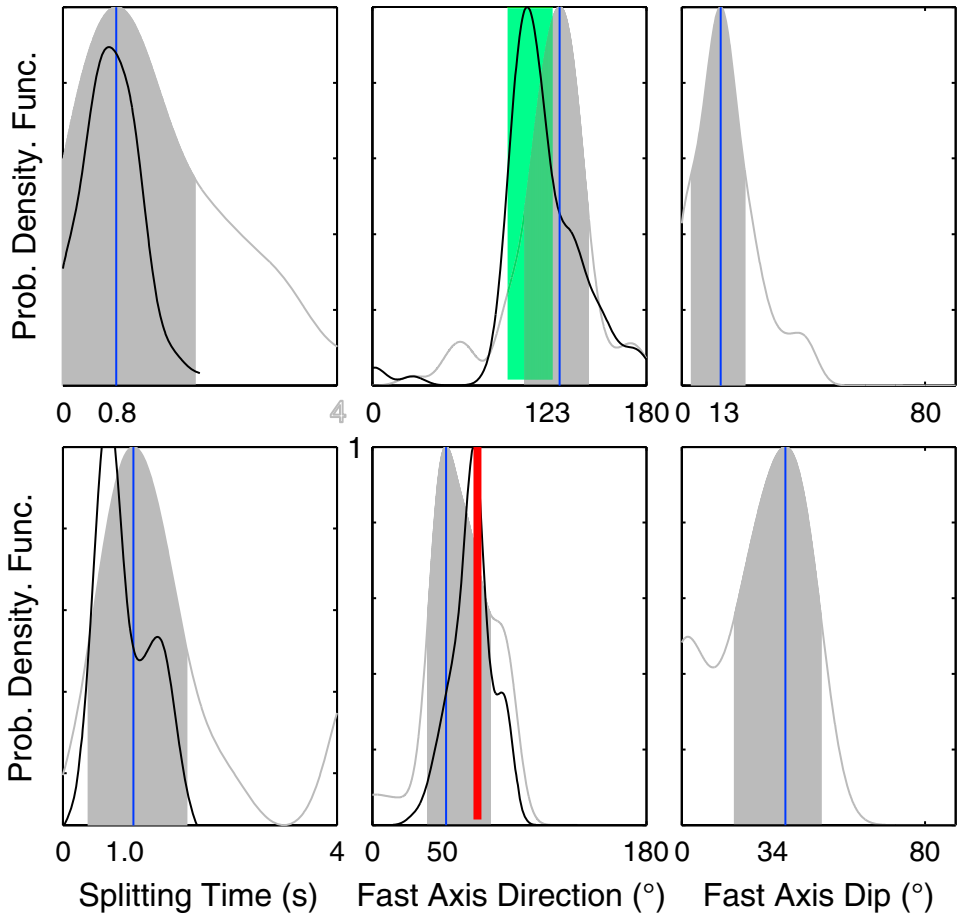


**Figure 10.** Two-layer modeling results for HRV station: (left column) splitting time, (middle column) fast axis direction, and (right column) fast axis plunge. The top and bottom panels are for the top and bottom layers, respectively. The gray lines and shades are for models which allow the fast axis diction to plunge (dip angle, right column). Thin black lines are for models with horizontal fast axis only for comparison. Blue vertical lines indicate the overall best model. The APM in the hotspot frame is indicated as red vertical line in the bottom layer. Green shaded region in the top layer shows the back azimuth, where systematic polarity changes occur in the receiver functions (Figure 7).

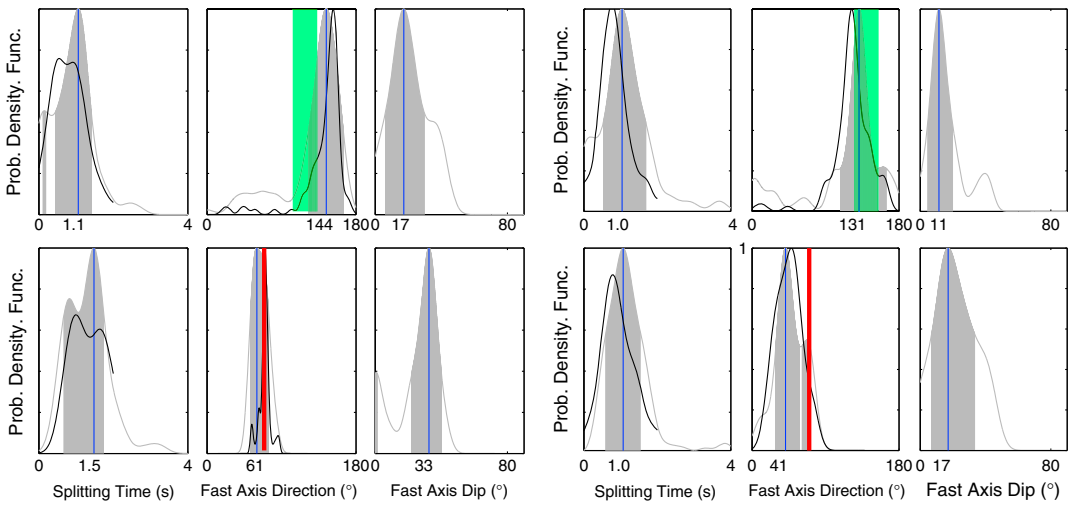


**Figure 11.** Same as in Figure 11 but for (left) PAL and (right) SSPA stations.

**Table 3.** Normalized *L*-2 Misfits and Model Significance[a]

| Station | One Layer | Two-Layer Flat | Two-Layer Dip |
|---|---|---|---|
| HRV | 1 | 1.0041 (53%) | 1.0723 (99%) |
| PAL | 1 | 1.2368 (99%) | 1.2432 (99%) |
| SSPA | 1 | 1.2477 (99%) | 1.2567 (99%) |

[a]Misfits are normalized to the one-layer case. Significance level (in percent) of the two-layer model fit compared to one layer is computed using the *F* test and assuming 1 depth of field/1 s *SKS* waveform.

each layer contributes nearly 1 s of splitting. The orientations of fast axes in two layers are close to orthogonal, and thus, there is a possibility of some trade-off in the model, with anisotropic effects of two layers cancelling each other. The presence of two nearly orthogonal systems of anisotropy is a plausible explanation for the broad range of splitting values reported when individual records are analyzed at this site [cf. *Liu*, 2009]. We note the overall consistency of the SSPA model with those for the other two sites (Figures 10 and 11) and include the values of parameters within it in our interpretation of the regional anisotropic structure.

To test whether the preferred two-layer anisotropy models are compatible with the single-layer "effective" values obtained from data, we carry out synthetic simulations for the three sites. We use the preferred two-layer models for each site (Figures 10 and 11) to simulate synthetic seismograms for the combinations of slownesses and back azimuths present in the real data set. The two-layer models used in the simulations are similar to that shown in Table 3, but with the top layer thickness and anisotropy strength scaled to match the ~10 s *P-SH* signal in the receiver functions. The structure likely responsible for this signal is discussed in detail in the following section. The reflectivity algorithm [*Levin and Park*, 1997] is used to simulate radial and transverse anisotropic responses for an incident *SV* phase, using slowness and back-azimuth values for the data at each of the sites analyzed. We then carry out a search for the single-layer apparent splitting parameters using bootstrap procedures and model space search criteria employed for real data. We present the distributions of anisotropic parameters for the resulting single-layer solutions in Figure 12.

Search results using synthetic data largely reproduce the distribution pattern found in the real data. Distributions of fast axis directions at all the three sites closely (within 20°) follow those obtained from data and show a similar

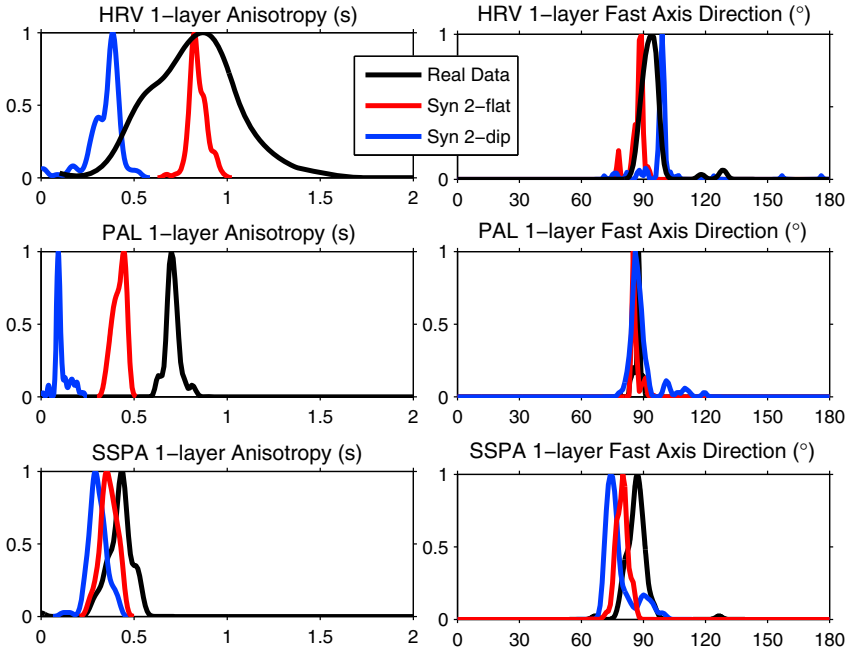


**Figure 12.** *SKS* synthetic modeling results. The input models are taken from Figures 10 and 11: (red) two-layer with horizontal fast axis and (blue) two-layer with dipping fast axis. Shown are distributions for single-layer apparent splitting parameters: (left) splitting time and (right) fast axis directions. Real data modeling results (black) are also plotted for comparison.

**Table 4.** RF Synthetic Models[a]

| Layer Depth (km) | *Vp* (km/s) | *Vs* (km/s) | Density (kg/m$^3$) | Anisotropy (%) | Axis Direction | Axis Plunge |
|---|---|---|---|---|---|---|
| | | | Model 1 | | | |
| 37 | 6.4 | 3.6 | 2650 | - | | |
| 50 | 8.1 | 4.6 | 3300 | - | | |
| 90 | 8.1 | 4.6 | 3300 | 8 | 120°SE | 35° |
| 120 | 7.7 | 4.2 | 3100 | - | | |
| Half space | 8.1 | 4.6 | 3300 | - | | |
| | | | Model 2 | | | |
| 37 | 6.4 | 3.6 | 2650 | - | | |
| 90 | 8.1 | 4.6 | 3300 | 8 | 144°SE | 17° |
| 170 | 8.1 | 4.6 | 3300 | 5 | 60°NE | 30° |
| Half space | 8.1 | 4.6 | 3300 | - | | |

[a]Parameters of models used in simulations of body wave conversion in anisotropic medium. Model 1 is based on previously published results as well as the features of the data. Model 2 is based on anisotropy parameters constrained though an inversion of *SKS* waveforms. Models start at 0 km depth and extend downward. The lowest layer is assumed to be an infinite half-space. Depths of layers given in the table signify their bottoms. Anisotropy is assumed to be hexagonally symmetric, and only cos 2φ terms are nonzero. Same values of anisotropy are assumed for both *P* and *S* waves. The $\varphi$ is the angle between the ray propagation direction and the axis of symmetry. See *Levin and Park* [1997, 1998] for details of the anisotropic medium description.

spread. The splitting times are smaller, especially in the dipping fast axis case. This may indicate that the real anisotropy strength may be higher or that more complex but vertically coherent structure is needed. The spread of splitting times at HRV is much narrower than in the real data, but is similar to the data distribution at SSPA and PAL, suggesting that the noise due to high levels of microseisms at HRV may have affected the data inversion. Overall, our synthetic experiment confirms that our preferred two-layer models of anisotropy predict split shear waves that will yield an effective fast polarization consistent with real data.

## 5. Predicting *P-SH* Conversions With Synthetic Seismograms

A prominent directionally variable *SH*-polarized receiver function phase at ~10 s delay (Figures 6 and 7) may be explained as a result of a *P*-to-*S* conversion at a boundary between two layers, with at least one being anisotropic. To test whether the observed directional variation patterns in our data are consistent with the expectations of the seismic structure at the LAB, we compute synthetic seismograms simulating plane wave propagation in layered anisotropic media and derive synthetic RFs from them. We use the PAL site data set as a template, preserving geometry of the observed earthquakes when computing synthetic seismograms. The reflectivity algorithm of *Levin and Park* [1997] is used to simulate three-component synthetic time series, from which receiver functions are subsequently produced using the same procedures as in real data analysis.

For the simulation, we construct a horizontally stratified velocity profile of the crust and the upper mantle to match the timing of most prominent phases, the positive phase on the radial component at ~5 s, and a polarity-reversed pulse at ~10 s on the transverse component. We also take into account the key results from past studies in the region, especially those [e.g., *Rychert et al.*, 2007] that employed converted waves to detect and characterize the LAB structure. Our very simple model has a one-layer crust, 37 km thick, a mantle lithosphere extending down to 90 km, and a thin layer of low velocity beneath the lithosphere. In the lower part of the mantle lithosphere, we introduce a single layer of anisotropy, with a symmetry axis chosen in such a way that *P-SH* converted wave would change its polarity at a back azimuth of ~120°SE. Table 4 lists all the parameters of the model. We compare the patterns of predicted and observed receiver functions in Figure 13. The key targets of the simulation, the radial pulse at ~5 s and a polarity reversed transverse pulse at 10 s, are matched quite well. Also, some secondary features seen in the data are matched as well, for example, a negative phase seen at ~7 s on the radial component and the timing and polarity (but not the absolute amplitude) of the pulses at ~7 s on the transverse. Some data features, e.g., a polarity-reversed phase at ~5 s, likely associated with the crust-mantle boundary, are not predicted at all as we chose to focus our attention on the features related to the LAB.

Testing the relative importance of various elements of the model we have constructed, we find that a large impedance contrast at the LAB (velocity decreasing down) is necessary for a sufficiently large SH-polarized phase at ~10 s to appear. The axis of symmetry in the anisotropic material directly above the LAB has to point in the

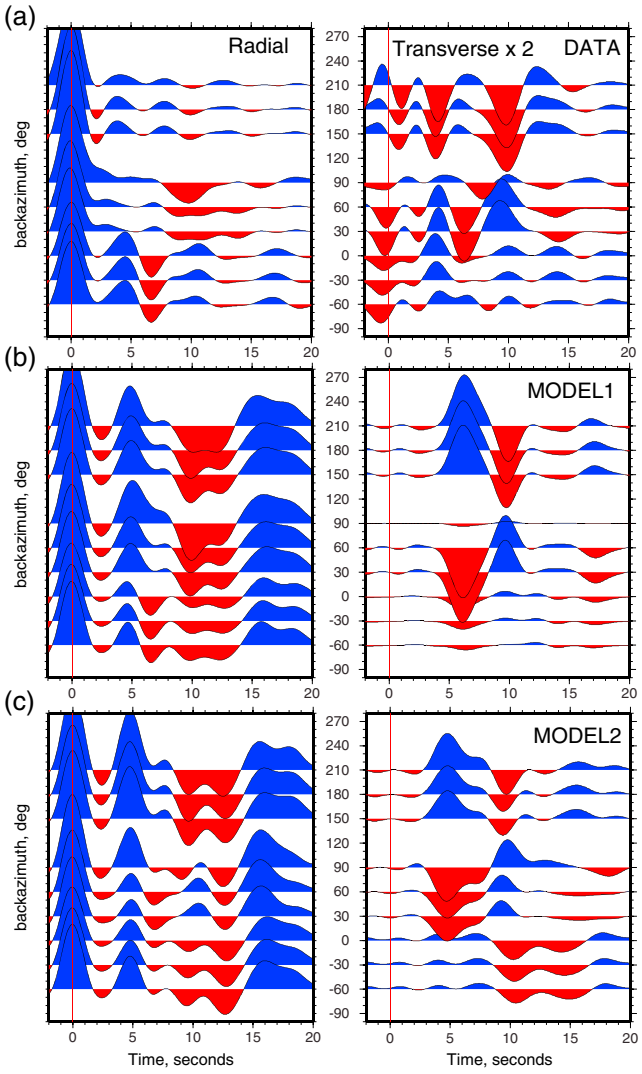


**Figure 13.** Receiver function synthetic tests for our preferred (b) model 1 and an alternative (c) model 2 in Table 4. (left column) The radial receiver function gathers and (right column) the transverse receiver function gathers. (a) Real data gathers are plotted for comparison.

direction along which the phase changes polarity (~120°SE) and to dip significantly from the horizontal. The combination of observed polarities is matched by the axis dip to the SE. Finally, the depth to the crust-mantle boundary (37 km) is determined in part by the choice of global average *Vp* and *Vs* speeds in the crust (6.4 and 3.6 km/s, respectively, for *P* and *S* waves). The mismatched features are instructive as well. We can see that the *SV*-polarized crustal multiples predicted between 10 and 15 s are not present in the data. This suggests the complexity of the crust-mantle boundary, also hinted at by the directional variation in the *P-SV* conversion at ~5 s in real RFs. The *SH*-polarized pulse at ~7 s originates at the top of the anisotropic layer in the lithosphere and is much larger than that observed. This points to the likely gradual upward decrease in rock fabric strength within the lithosphere. The timing of this pulse is consistent with the phases interpreted as marking the MLD [*Rychert et al.*, 2007], suggesting that the changes in anisotropy may be the underlying cause for it.

To test the sensitivity of the *P-SH* converted wave data to the presence of deep anisotropic layer suggested by the *SKS* inversion, we carry out a second receiver function simulation (Figure 13c). We use a model based on the results of the *SKS* data inversion for site PAL. Specifically, we introduce two anisotropic layers in the mantle, with fast symmetry axis parameters (directions and dips) taken from the *SKS* inversion and with layer thicknesses and strengths of anisotropy chosen so that splitting delays in each are matched. We use an approximate rule that a shear wave propagating through ~100 km of material with ~4% anisotropy will accumulate ~1 s of "splitting delay" between differently polarized components [*Silver*, 1996]. There is no low-velocity layer in the second model; thus, *P*-to-*SH* converted phases at ~10 s delay arise from the changes in anisotropic parameters. For these phases to appear, the change in anisotropic parameters with depth needs to be abrupt. In the case of our model, the layers with distinct anisotropy are in direct contact, a condition that is in agreement with, but not required, by the *SKS* data.

Resulting patterns of *P-SV* and *P-SH* converted phases (Figure 13c) display some of the features seen in the first simulation (Figure 13b), and in the data, such as the *P-SV* positive conversion at ~5 s and a *P-SH* phase at ~10 s with a switch in polarity at ~120°SE. This transverse phase also has a second polarity change between directions 0 and 30°NE, a feature not observed in the data. Also, not observed in the data are the strong *P-SV* polarized multiples between 13 and 17 s, originating from the sharp crust-mantle transition. On the transverse component of the synthetic RFs, a polarity reversing phase at ~5 s displays a pattern very different

from that seen in data. This phase originates from a contact of the upper anisotropic layer and the isotropic crust above it.

In addition to phases arising at the boundaries of the upper anisotropic layer, a group of *P-SH* conversions predicted at ~15 s show a polarity change pattern similar, but not identical, to that observed. A comparison with the pattern simulated in the first receiver function model (Figure 13b; where there is no second layer of anisotropy) suggests that at least some energy at this delay time arises from crustal multiples.

Overall, the match between synthetics predicted in a model based on *SKS* data inversion is not as good as that in a simpler model 1 based on isotropic velocity profiles from *Rychert et al.* [2007]. In particular, contributions from the deeper anisotropic layer add features not seen in the data. Thus, we think it is unlikely that the anisotropic layers inferred from the *SKS* modeling are in direct contact. Also, our simulations suggest that the lower layer of anisotropy is bounded by smooth rather than abrupt changes in properties.

A comparison of the models we have tried (Figures 13b and 13c) suggests that the pattern of *P-SH* conversion at ~10 s is controlled primarily by the properties of the material above it. At the same time, either a low-velocity zone or an abrupt change in anisotropy at ~90 km depth is required to produce a *P-SH* conversion of sufficient size.

Strong anisotropy necessary to predict a large *P-SH* converted phase at ~10 s leads to the formation of a set of polarity-reversed pulses from the upper bound of the anisotropic layer. We do not find correspondingly strong phases in data, which suggest a vertical variation in anisotropy strength. While high levels of anisotropy (8%) are required at the lower boundary of the layer, lack of corresponding features from the upper boundary implies a gradual decrease of anisotropy upward. A structure like this has previously been proposed for the Arabian shield by *Levin and Park* [2000]. Relatively weak *P-SH* converted phases observed at 6–7 s delay may be related to the upper limit of anisotropic material, or to a localized variation in anisotropy strength. The presence of a clear polarity-reversed *P-SH* pulse at ~5 s in the data implies that anisotropic features have to reside close to the crust-mantle boundary. The symmetry of anisotropy causing these features is likely similar to that at the 90 km boundary.

To summarize, our examination of *P*-to-*SV* converted waves reveals features familiar from previous work by *Rychert et al.* [2007], while our work on *SH*-polarized component of receiver functions allows us to probe the anisotropic velocity structure in a new way. The key observation is a strong and regionally consistent *SH*-polarized converted phase that arrives at ~10 s delay, with a polarity change at back azimuth ~120–140°SE (Figure 7). This delay leads us to associate the phase with the LAB proposed at 90–100 km in the region [*Rychert et al.*, 2007; *Abt et al.*, 2010]. Frequency content of the phase (Figures 7 and 13) offers an insight into the sharpness of the gradient in properties necessary for producing it. The phase is clear at ~2 s period (Figure 7). Assuming a shear wave speed of 4.6 km/s and invoking the the quarter-wavelength rule [*Widess*, 1973], we can estimate the width of the impedance and/or fabric change at 2–3 km. Forward modeling of RFs carried out in this study is guided by the Occam's Razor principle; in that, we seek a model that fits our observations with the least amount of complexity. We stress that in the RF modeling, we are not "inverting" for a model (as we do for *SKS* data) but rather are testing models suggested by *SKS* inversions and by previously published results.

## 6. Discussion

### 6.1. Consistent Constraints on Anisotropic Distribution With Depth

We compare the attributes of seismic anisotropy in the upper mantle beneath our study region inferred from three different methods. Previously published constraints from the surface wave inversion [*Yuan et al.*, 2011] suggest the presence of two distinct fabrics at different depth (Figure 2). The upper region of fabric is above ~150 km, with a peak anisotropy strength at ~100 km. The fast propagation direction for shear waves within this region is rotated 40–60° clockwise from the APM. The lower region of fabric resides below ~200 km and has the fast shear wave propagation direction closely aligned with the APM.

The study of *SKS* phases at the three sites separated by distances ~200 km yields very similar models of vertical distribution in anisotropic properties. At all the three locations (HRV, PAL, and SSPA), data favor at least two layers of anisotropic material with distinct properties (Figures 10 and 11). Fast axes of anisotropic

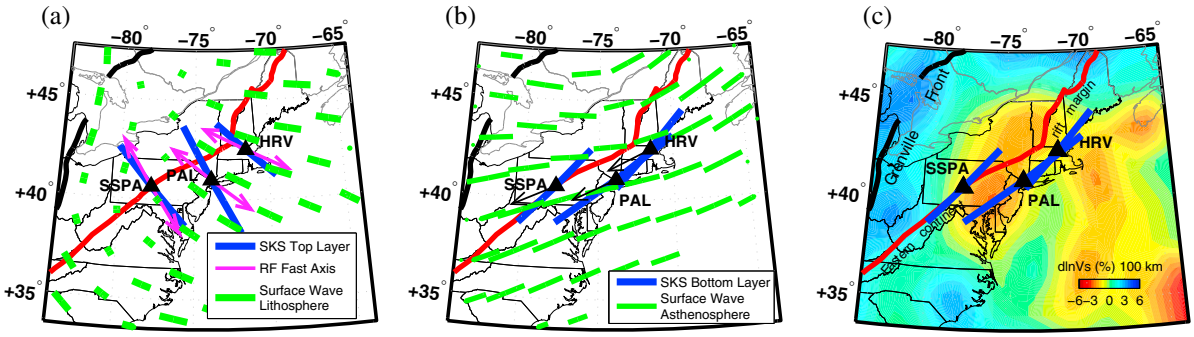


**Figure 14.** Map view showing the two-layer modeling results for the (a) top layer and (b) bottom layer. The lithosphere anisotropy direction inferred from transverse receiver functions is also plotted as arrows in Figure 14a. The top and bottom layer splitting times are scaled according to Figures 11 and 12. Green sticks in Figures 14a and 14b are the equivalent two-layer (lithosphere and asthenosphere) apparent splitting predictions from the 3-D azimuthal anisotropy model of *Yuan et al.* [2011], maximum 1 s in the bottom layer. (c) *Vs* variation from *Yuan et al.* [2014]. Black arrows in Figure 14b show the APM direction in the HS3-NUVEL 1A model. The bottom layer *SKS* modeling results are also shown in Figure 14c for comparison. Black arrows in Figure 14b show the APM direction in the HS3-NUVEL 1A model. The bottom layer *SKS* modeling results are also shown in Figure 14c for comparison.

symmetry in the upper layer of the best fitting models are in the range of 120°–145°SE and plunge gently from the vertical. In the lower layers of all models, fast axes are in the 40°–60°NE range and plunge by more than 30° from the horizontal. The strength of anisotropy, expressed as the amount of delay in individual model layers, is on the order of ~1 s in all. For anisotropy at 4% level, this would translate into ~100 km of anisotropic upper mantle rock [*Silver*, 1996]; however, due to a complete trade-off in anisotropy strength and layer thickness, *SKS* data allow for both thinner, more anisotropic layers and thicker, less anisotropic ones. Lateral separation of our three sites precludes significant overlap in the volumes sampled by their data. Thus, we infer significant continuity in anisotropic structure over the area.

An examination of the *P-SH* converted waves at the same three sites shows that their directional variation is very similar (Figure 7). To match this variation, an abrupt boundary in anisotropic properties is required at ~90 km depth. Anisotropy with a fast axis of symmetry pointing ~120°SE and plunging by 35° from the horizontal predicts the observed pattern well. Aspects of the receiver function wavefield (Figures 7 and 13) suggest that anisotropy is not uniform with depth. As with the *SKS* phases, near-vertical illumination by the *P-SH* converted phases assures little, if any, overlap of the volumes sampled beneath the three sites in the upper mantle. Once again, we find evidence for lateral continuity of anisotropic velocity structure at depth.

We summarize all of the above constraints in Figure 14, showing anisotropic symmetry axes predicted by *SKS* and RF observations at the three stations and fast axis directions predicted for the lithosphere and the asthenosphere in the *Yuan et al.*'s [2011] continent-scale model. On the basis of close agreement we see in orientations of fast directions at different depth levels, we define two distinct anisotropic layers in the upper mantle: an upper lithospheric layer with a fast direction ~120°SE and an asthenospheric layer with a fast direction ~50°NE. It should be noted that there is an internal heterogeneity within each, as specific values of anisotropy parameters vary from location to location. This is especially pronounced in the strength of anisotropy predicted in the lithosphere part of the *Yuan et al.*'s [2011] model, which gets progressively smaller from the coast inland. Nevertheless, the differences between these two layers are significantly larger than the internal variation within each.

### 6.2. Flow-Induced Anisotropy in the Asthenosphere

Fast direction of anisotropy in the deeper part of the upper mantle aligns closely, although not exactly, with the directions of North American plate motion in the hotspot reference frame [*Gripp and Gordon*, 2002]. Data types favoring this result are the *SKS* splitting and surface wave dispersion, while mode-converted body waves do not require it. The model developed by *Yuan et al.* [2011] is based on both surface wave waveforms and *SKS* splitting data, with the latter being introduced in the form of a single set of two parameters, fast direction, and delay, for each site included. As station averaged values, such parameterization of *SKS* observations naturally excludes directional variations in them [*Romanowicz and Yuan,* 2012]. The treatment of *SKS* records in the inversions carried out in this paper is philosophically different; in that, data records are matched by predictions from models rather than "analyzed" for the attributes of their particle motion reflecting anisotropy. The variation of time series as a function of back azimuth is a key aspect being matched

in the inversion. Because of these considerations, we believe that the local constraints on the anisotropic velocity distribution at the three sites are independent of the parameters of the continent-wide inversion of *Yuan et al.* [2011]. We envisage using such independent constraints on the anisotropic structure in the future generation of models like that of *Yuan et al.* [2011].

The match between the two estimates of the fast shear wave direction in the asthenosphere is far from perfect (Figure 14b). Relative to the *SKS*-based estimates, the fast direction predicted from the *Yuan et al.*'s [2011] model is consistently rotated clockwise by ~20°. A likely cause of it is the limited lateral resolution of the continent-scale model, as discussed in the introduction section of the paper. The region of study has a relatively small-scale lateral variation in upper mantle properties (e.g., Figure 14c) and thus averaging over ~500 km in *Yuan et al.*'s [2011] model likely biases the local results. While the close alignment of fast directions with APM vectors is in many regards an expected result [cf. *Vinnik et al.*, 1998], the ~20° angular difference between the two estimates is likely due to the perturbation in the asthenosphere flow induced by the LAB topography: the lithosphere is thinner than the surrounding areas, as indicated by slower shear velocities (Figure 14c) beneath the stations [e.g., *van der Lee*, 2002; *Li et al.*, 2003; *Yuan et al.*, 2014]. Given much more complex patterns of shear wave splitting reported to the south of our study area [*Long et al.*, 2010; *Wagner et al.*, 2012], it is an important constraint on the upper mantle dynamics of eastern North America. Unlike the southern Appalachian coastal plain investigated by *Long et al.* [2010] and *Wagner et al.* [2012], our study region shows no evidence for predominantly vertical mantle flow.

### 6.3. Likely Causes for the Orientation of Lithospheric Anisotropy

Our findings support the view of the North American continental lithosphere as a layered object with multiple internal boundaries [*Yuan and Romanowicz*, 2010]. All the three methods we use to probe the anisotropic properties concur on the orientation of the fast shear wave speed within it being ~120–140°SE. Surface wave results (Figures 2 and 14) suggest that the strength of this fabric varies laterally, while modeling of receiver function patterns at PAL (Figure 13) points to the variations in fabric strength in the vertical direction. Three aspects of lithospheric anisotropy are especially notable. First, it is broadly consistent over a large region. In the present study, we find it at three sites 200 km apart, while earlier studies by *Levin et al.* [1999, 2000] reported similar anisotropic properties under most of New England. Second, the fast direction in the lithosphere is at a high angle to the strike of major tectonic units in the region. Third, the lower bound of the lithosphere appears to be sharp, and the anisotropy associated with it is strong. The large lateral extent of similar anisotropic properties suggests a regional deformation event that affected a large fraction of the present-day northern Appalachians. What this event may have been is an open question at the moment. *Thomas* [2006] discusses numerous episodes of tectonism along the Atlantic coast of North America and argues for "inheritance" in the location and orientation of major tectonic features. However, while there is a range of candidate tectonic episodes in North American continent's history that could have imparted oriented rock fabric onto its mantle lithosphere, most could not form the fabric oriented in the SE-NW direction.

Specifically, deformation related to the assembly of the Appalachians from a set of terranes [*Williams and Hatcher*, 1982; *Hibbard et al.*, 2007] is not a plausible candidate. Numerous studies [e.g., *Vauchez and Nicholas*, 1991; *Silver et al.*, 2004] noted near-parallel directions of tectonic units in compressive orogens and the fast direction of anisotropy and argued for orogen-parallel flow. Similarly, it is difficult to relate the broadly distributed subhorizontal deformation to the rifting of the Atlantic, which was highly focused in the area presently offshore [*Holbrook and Kelemen*, 1993]. Furthermore, studies of modern rifts [e.g., *Gao et al.*, 1994; *Bastow et al.*, 2010] commonly find rift-parallel fast shear wave directions.

A scenario that may explain the observed aspects of lithospheric anisotropy would involve a loss, on a regional scale, of the lower part of the lithosphere. This episode has to occur after the assembly of the Appalachians so as to impact all the terranes involved. In an earlier paper [*Levin et al.*, 2000], we considered a possibility of viscous instability [e.g., *Houseman and Molnar*, 1997; *Pysklywec*, 2001;] that would lead to the development of intense deformation in the depth range where the lithosphere detaches. Models of continental lithosphere deformation and destabilization, reviewed in detail by *Pysklywec et al.* [2010], consistently show narrow subhorizontal zones of intense deformation ("stretch marks") forming in areas where mantle lithosphere detaches and sinks. Given the broad aerial presence of the lithospheric fabric, we believe that a "delamination" in the original sense, as proposed by *Bird* [1979], may be more applicable. Unlike

the original proposition by *Bird* [1979], this delamination must have occurred along a weak zone within the lithosphere, not at the crust-mantle boundary. The surface along which the delamination took place would become the new LAB, sharply bounded against underlying asthenosphere, and with strong deformation-induced fabric in its lower part. The region of reduced seismic wave speed at 100 km (Figure 14c) corresponds to the area where our past and present studies of shear wave splitting identified two-layered anisotropy structure and includes most of the "confident" LAB determinations in a study by *Abt et al.* [2010]. We propose that this region corresponds to the area where the lower part of the lithosphere has delaminated at some point after the formation of the Appalachians.

## 7. Summary

We examined the data of two different types that offer complementary constraints on seismic anisotropy distribution in the upper mantle. Both types of data were previously used in this region, by us and by other researchers [*Barruol et al.*, 1997; *Levin et al.*, 1999; *Fouch et al.*, 2000; *Liu*, 2009; *Rychert et al.*, 2005, 2007; *Abt et al.*, 2010]. We revisit these data applying different types of analysis. We focus on the *P*-to-*SH* conversion in the receiver function analysis, which we predict using forward modeling in simple layered structures; and we use group inversion of *SKS* records to derive vertical profiles of anisotropic properties. Also, we benefit from additional data having accumulated at the sites we examine, allowing us a luxury of using larger events with higher signal-to-noise ratio.

A key result of our study is the agreement we find between the three different methods of constraining seismic anisotropy in the upper mantle. Regional anisotropic parameters in the continent-wide model of *Yuan et al.* [2011] are verified both by models predicting shear wave splitting at three sites and by anisotropy-aware receiver functions developed for the same three sites.

Our specific findings are as follows:

1. Both *SKS* and *P-S* converted phases favor a presence of anisotropic material with a fast axis oriented ~120° SE in the upper part of the mantle. Receiver functions suggest a sharp lower bound of this material at 90 km. *SKS* splitting implies a cumulative strength on the order of 8% given the likely ~50 km thickness of the material that is anisotropic and the size of the delay (~1 s) inferred within it.
2. Receiver functions require the axis of symmetry to dip in the vicinity of the lower boundary of the lithosphere. The pattern of observed *P-S* conversions excludes the possibility of the entire lithospheric depth range having uniform anisotropy, so a likely scenario is that of vertically variable rock fabric. To produce the amount of *SKS* splitting inferred from the modeling, the degree of anisotropy has to be very high in some part of the 37 to 90 km depth range.
3. *SKS* data support the presence of a second layer of anisotropy predicted by the *Yuan et al.*'s [2011] model; however, its presence is not obvious in the receiver function data. A plausible explanation is that there are no abrupt changes in this deeper rock fabric layer—a scenario consistent with it being formed by present-day viscous flow.
4. The inferred lithospheric anisotropy fast axis direction is at a high angle to the strike of major tectonic units in the Appalachians and is nearly identical over a broad region. Among the possible tectonic events that may have imparted such fabric on the lithosphere, we favor a loss (delamination) of the lower lithosphere on a regional scale at some point after the formation of the Appalachian orogen.
5. The close alignment of fast directions in the second layer of anisotropy with APM vectors is an anticipated result. In the eastern North American, our observation favors the APM directions in the hotspot frame.

Finally, we would like to stress the importance of long-term observations, and the efficient archiving, of seismic data—both analyses we have carried out in this work would not be possible without nearly 2 decades of continuous data being readily available for the three test sites.

**Acknowledgments**
We thank the IRIS DMC for providing waveforms for the receiver function and SKS analyses in this study. Two anonymous reviewers and the Editor are thanked for their constructive comments to improve the manuscript. Generic Mapping Tools [*Wessel and Smith*, 1991] were used to draft many of the figures. V.L. is grateful to Rutgers University for a sabbatical leave that allowed him to focus on this work. H.Y. acknowledges the support by iVEC through the use of advanced computing resources located at the Pawsey Center, Australia. This is contribution 445 from the ARC Centre of Excellence for Core to Crust Fluid Systems (http://www.ccfs.mq.edu.au).

## References

Abt, D. L., K. M. Fischer, S. W. French, H. A. Ford, H. Yuan, and B. Romanowicz (2010), North American lithospheric discontinuity structure imaged by Ps and Sp receiver functions, *J. Geophys. Res.*, *115*, B09301, doi:10.1029/2009JB006914.

Artemieva, I. M. (2009), The continental lithosphere: Reconciling thermal, seismic, and petrologic data, *Lithos*, *109*, 23–46.

Barruol, G., P. G. Silver, and A. Vauchez (1997), Seismic anisotropy in the eastern United States: Deep structure of a complex continental plate, *J. Geophys. Res.*, *102*, 8329–8348.

Bastow, I. D., S. Pilidou, J.-M. Kendall, and G. W. Stuart (2010), Melt-induced seismic anisotropy and magma assisted rifting in Ethiopia: Evidence from surface waves, *Geochem. Geophys. Geosyst.*, *11*, Q0AB05, doi:10.1029/2010GC003036.
Bird, P. (1979), Continental delamination and the Colorado Plateau, *J. Geophys. Res.*, *84*(B13), 7561–7571.
Bodin, T., H. Yuan, and B. Romanowicz (2014), Inversion of receiver functions without deconvolution—application to the Indian craton, *Geophys. J. Int.*, *196*(2), 1025–1033, doi:10.1093/gji/ggt431.
Bostock, M. G. (1997), Anisotropic upper-mantle stratigraphy and architecture of the Slave craton, *Nature*, *390*, 392–395.
Bostock, M. G. (1998), Mantle stratigraphy and evolution of the Slave Province, *J. Geophys. Res.*, *103*, 21,183–121,200.
Chen, C.-W., S. Rondenay, R. L. Evans, and D. B. Snyder (2009), Geophysical detection of relict metasomatism from an Archean (~3.5 Ga) Subduction Zone, *Science*, *326*, 1089–1091.
Cooper, C. M., A. Lenardic, and L. Moresi (2004), The thermal structure of stable continental lithosphere within a dynamic mantle, *Earth Planet. Sci. Lett.*, *222*, 807–817.
Cooper, C. M., and M. S. Miller (2014), Craton formation: Internal structure inherited from closing of the early oceans, *Lithosphere*, *6*(1), 35–42, doi:10.1130/l321.1.
DeMets, C., R. G. Gordon, D. F. Argus, and S. Stein (1994), Effect of recent revisions to the geomagnetic reversal time scale on estimates of current plate motions, *Geophys. Res. Lett.*, *21*, 2191–2194.
Eaton, D. W., F. Darbyshire, R. L. Evans, H. Grütter, A. G. Jones, and X. Yuan (2009), The elusive lithosphere-asthenosphere boundary (LAB) beneath cratons, *Lithos*, *109*, 1–22.
Efron, B., and R. Tibshitani (1986), Bootstrap methods for standard errors, confidence intervals, and other measures of statistical accuracy, *Stat. Sci.*, *1*, 54–77.
Fischer, K. M., H. A. Ford, D. L. Abt, and C. A. Rychert (2010), The lithosphere-asthenosphere boundary, *Annu. Rev. Earth Planet. Sci.*, *38*, 551–575.
Fouch, M. J., K. M. Fischer, E. M. Parmentier, M. E. Wysession, and T. J. Clarke (2000), Shear wave splitting, continental keels, and patterns of mantle flow, *J. Geophys. Res.*, *105*, 6255–6275.
Fouch, M. J., and S. Rondenay (2006), Seismic anisotropy beneath stable continental interiors, *Phys. Earth Planet. Inter.*, *158*(2–4), 292–320.
Ford, H. A., K. M. Fischer, D. L. Abt, C. A. Rychert, and L. T. Elkins-Tanton (2010), The lithosphere-asthenosphere boundary and cratonic lithospheric layering beneath Australia from Sp wave imaging, *Earth Planet. Sci. Lett.*, *300*, 299–310.
Frederiksen, A. W., and M. G. Bostock (2000), Modelling teleseismic waves in dipping anisotropic structures, *Geophys. J. Int.*, *141*(2), 401–412, doi:10.1046/j.1365-246x.2000.00090.x.
Gao, S., P. M. Davis, H. Liu, P. D. Slack, Y. A. Zorin, V. V. Mordvinova, V. M. Kozhevnikov, and R. P. Meyer (1994), Seismic anisotropy and mantle flow beneath the Baikal rift zone, *Nature*, *371*(6493), 149–151.
Grand, S. P., and D. V. Helmberger (1984), Upper mantle shear structure of North America, *Geophys. J. Int.*, *76*, 399–438.
Green, D. H., W. O. Hibberson, I. Kovacs, and A. Rosenthal (2010), Water and its influence on the lithosphere-asthenosphere boundary, *Nature*, *467*, 448–451.
Griffin, W. L., S. Y. O'Reilly, B. J. Doyle, N. J. Pearson, H. Coopersmith, K. Kivi, V. Malkovets, and N. Pokhilenko (2004), Lithosphere mapping beneath the North American plate, *Lithos*, *77*, 873–922.
Gripp, A. E., and R. G. Gordon (2002), Young tracks of hotspots and current plate velocities, *Geophys. J. Int.*, *150*, 321–361.
Gung, Y., M. Panning, and B. Romanowicz (2003), Global anisotropy and the thickness of continents, *Nature*, *422*(6933), 707–711.
Hibbard, J. P., C. R. van Staal, and D. W. Rankin (2007), A comparative analysis of pre-Silurian crustal building blocks of the northern and the southern Appalachian Orogen, *Am. J. Sci.*, *307*, 23–45.
Holbrook, W. S., and P. B. Kelemen (1993), Large igneous province on the US Atlantic margin and implications for magmatism during continental breakup, *Nature*, *364*(6436), 433–436.
Houseman, G. A., and P. Molnar (1997), Gravitational (Rayleigh-Taylor) instability of a layer with non- linear viscosity and convective thinning of conti- nental lithosphere, *Geophys. J. Int.*, *128*, 125–150.
Jones, A. G., P. Lezaeta, I. J. Ferguson, A. D. Chave, R. L. Evans, X. Garcia, and J. Spratt (2003), The electrical structure of the Slave craton, *Lithos*, *71*(2–4), 505–527.
Karato, S.-I. (2012), On the origin of the asthenosphere, *Earth Planet. Sci. Lett.*, *321–322*, 95–103.
Kawakatsu, H., P. Kumar, Y. Takei, M. Shinohara, T. Kanazawa, E. Araki, and K. Suyehiro (2009), Seismic evidence for sharp lithosphere-asthenosphere boundaries of oceanic plates, *Science*, *324*, 499–502.
Kumar, P., R. Kind, X. Yuan, and J. Mechie (2012), USArray receiver function images of the lithosphere-asthenosphere boundary, *Seismol. Res. Lett.*, *83*, 486–491.
Langston, C. A. (1977), Corvallis, Oregon, crustal and upper mantle receiver structure from telesismic P and S waves, *Bull. Seismol. Soc. Am.*, *67*, 713–724.
Lay, T. (Eds.) (2009), Seismological Grand Challenges in Understanding Earth's Dynamic Systems. report to the National Science Foundation, IRIS consortium, 76 pp.
Levander, A., B. Schmandt, M. S. Miller, K. Liu, K. E. Karlstrom, R. S. Crow, C. T. A. Lee, and E. D. Humphreys (2011), Continuing Colorado plateau uplift by delamination-style convective lithospheric downwelling, *Nature*, *472*(7344), 461–465.
Levin, V., and J. Park (1997), P-SH conversions in a flat-layered medium with anisotropy of arbitrary orientation, *Geophys. J. Int.*, *131*, 253–266.
Levin, V., and J. Park (1998), P-SH conversions in layered media with hexagonally symmetric anisotropy; a cookbook, *Pure Appl. Geophys.*, *151*, 669–697.
Levin, V., and J. Park (2000), Shear zones in the Proterozoic lithosphere of the Arabian Shield and the nature of the Hales discontinuity, *Tectonophysics*, *323*, 131–148.
Levin, V., W. Menke, and J. Park (1999), Shear wave splitting in the Appalachians and the Urals; a case for multilayered anisotropy, *J. Geophys. Res.*, *104*, 17,975–917,994.
Levin, V., J. Park, M. Brandon and W. Menke (2000), Thinning of the upper mantle during the late Paleozoic Appalachian orogenesis, *Geology*, *28*, 239–242.
Levin, V., A. Henza, J. Park, and A. Rodgers (2006), Texture of mantle lithosphere along the Dead Sea Rift: recently imposed or inherited?, *Phys. Earth Planet. Inter.*, *158*(2–4), 174–189, doi:10.1016/j.pepi.2006.05.007.
Levin, V., S. Roecker, P. Graham, and A. Hosseini (2008), Seismic anisotropy indicators in Western Tibet: Shear wave splitting and receiver function analysis, *Tectonphysics*, doi:10.1016/j.tecto.2008.03.019.
Levin, V., G. D. Huang, and S. Roecker (2012), Crust-mantle coupling at the northern edge of the Tibetan plateau: Evidence from focal mechanisms and observations of seismic anisotropy, *Tectonophysics*, *584*(22), 221–229.

Li, A., D. W. Forsyth, and K. M. Fischer (2003), Shear velocity structure and azimuthal anisotropy beneath eastern North America from Rayleigh wave inversion, *J. Geophys. Res.*, *108*(B82362), doi:10.1029/2002JB002259.
Liu, K. H. (2009), NA-SWS-1.1: a uniform database of teleseismic shear wave splitting measurements for North America, *Geochem. Geophys. Geosyst.*, *10*, Q05011, doi:10.1029/2009GC002440.
Long, M. D., and T. W. Becker (2010), Mantle dynamics and seismic anisotropy, *Earth Planet. Sci. Lett.*, *297*, 341–354.
Long, M. D., M. H. Benoit, M. C. Chapman, and S. D. King (2010), Upper mantle anisotropy and transition zone thickness beneath southeastern North America and implications for mantle dynamics, *Geochem. Geophys. Geosyst.*, *11*, Q10012, doi:10.1029/2010GC003247.
Menke, W., and V. Levin (2002), Anomalous seaward dip of the lithosphere-asthenosphere boundary beneath northeastern US detected using differential-array measurements of Rayleigh waves, *Geophys. J. Int.*, *149*, 413–421.
Menke, W., and V. Levin (2003), The cross-convolution method for interpreting SKS splitting observations, with application to one and two-layer anisotropic earth models, *Geophys. J. Int.*, *154*, 379–392.
Mierdel, K., H. Keppler, J. R. Smyth, and F. Langenhorst (2007), Water solubility in aluminous orthopyroxene and the origin of Earth's asthenosphere, *Science*, *315*, 364–368.
Nettles, M., and A. M. Dziewonski (2008), Radially anisotropic shear velocity structure of the upper mantle globally and beneath North America, *J. Geophys. Res.*, *113*, B02303, doi:10.1029/2006JB004819.
Nikulin, A., V. Levin, and J. Park (2009), Receiver function study of the Cascadia megathrust: Evidence for localized serpentinization, *Geochem. Geophys. Geosyst.*, *10*, Q07004, doi:10.1029/2009GC002376.
O'Reilly, S. Y., and W. L. Griffin (2010), The continental lithosphere-asthenosphere boundary: Can we sample it?, *Lithos*, *120*(1–2), 1-–13, doi:10.1016/j.lithos.2010.03.016.
Park, J., and V. Levin (2000), Receiver functions from multiple-taper spectral correlation estimates, *Bull. Seismol. Soc. Am.*, *90*, 1507–1520.
Park, J., and V. Levin (2002), Seismic anisotropy: Tracing plate dynamics in the mantle, *Science*, *296*, 485–489.
Park, J., H. Yuan, and V. Levin (2004), Subduction zone anisotropy beneath Corvallis, Oregon: A serpentinite skid mark of trench-parallel terrane migration?, *J. Geophys. Res.*, *109*, B10306, doi:10.1029/2003JB002718.
Pysklywec, R. N. (2001), Evolution of subducting mantle lithosphere at a continental plate boundary, *Geophys. Res. Lett.*, *28*(23), 4399–4402.
Pysklywec, R. N., O. Gogus*, J. Percival, A. R. Cruden, and C. Beaumont (2010), Insights from geodynamical modeling on possible fates of continental mantle lithosphere: Collision, removal, overturn, *Can. J. Earth Sci.*(Lithoprobe Synthesis Volume), *47*(4), 541–563.
Ribe, N. M. (1992), On the relation between seismic anisotropy and finite strain, *J. Geophys. Res.*, *97*, 8737–8747.
Romanowicz, B. (2009), The thickness of tectonic plates, *Science*, *324*, 474–476.
Romanowicz, B., and H. Yuan (2012), On the interpretation of SKS splitting measurements in the presence of several layers of anisotropy, *Geophys. J. Int.*, *188*(3), 1129–1140, doi:10.1111/j.1365-246X.2011.05301.x.
Rychert, C. A., K. M. Fischer, and S. Rondenay (2005), A sharp lithosphere-asthenosphere boundary imaged beneath eastern North America, *Nature*, *436*, 542–545.
Rychert, C. A., S. Rondenay, and K. M. Fischer (2007), P-to-S and S-to-P imaging of a sharp lithosphere-asthenosphere boundary beneath eastern North America, *J. Geophys. Res.*, *112*, B08314, doi:10.1029/2006JB004619.
Rychert, C. A., and P. M. Shearer (2009), A global view of the lithosphere-asthenosphere boundary, *Science*, *324*, 495–498.
Sambridge, M. (1999a), Geophysical inversion with a neighbourhood algorithm—I. Searching a parameter space, *Geophys. J. Int.*, *138*, 479–494.
Sambridge, M. (1999b), Geophysical inversion with a neighbourhood algorithm—II. Appraising the ensemble, *Geophys. J. Int.*, *138*(3), 727–746, doi:10.1046/j.1365-246x.1999.00900.x.
Silver, P. G. (1996), Seismic anisotropy beneath the continents: Probing the depths of geology, *Annu. Rev. Earth Planet. Sci.*, *24*, 385–432.
Silver, P. G., M. J. Fouch, S. S. Gao, and K. S. Group (2004), The structure and evolution of Southern Africa: The view from an anisotropic mantle, *S. Afr. J. Geol.*, *107*, 45–58.
Sleep, N. H. (2009), Stagnant lid convection and carbonate metasomatism of the deep continental lithosphere, *Geochem. Geophys. Geosyst.*, *10*, Q11010, doi:10.1029/2009GC002702.
Thomas, W. A. (2006), Tectonic inheritance at a continental margin, *GSA Today*, *16*(2), doi:10.1130/1052-5173.
Thybo, H., and E. Perchuc (1997), The seismic 8° discontinuity and partial melting in continental mantle, *Science*, *275*, 1626–1629.
Thybo, H. (2006), The heterogeneous upper mantle low velocity zone, *Tectonophysics*, *416*, 53–79.
Van der Lee, S. (2002), High-resolution estimates of lithospheric thickness from Missouri to Massachusetts, USA, *Earth Planet. Sci. Lett.*, *203*, 15–23.
Vauchez, A., and A. Nicholas (1991), Mountain building: Strike-parallel motion and mantle anisotropy, *Tectonophysics*, *185*, 183–201.
Vinnik, L., S. Chevrot, and J. P. Montagner (1998), Seismic evidence of flow at the base of the upper mantle, *Geophys. Res. Lett.*, *25*, 1995–1998.
Wagner, L. S., M. D. Long, M. D. Johnston, and M. H. Benoit (2012), Lithospheric and asthenospheric contributions to shear-wave splitting observations in the southeastern United States, *Earth Planet. Sci. Lett.*, *341–344*(0), 128–138, doi:10.1016/j.epsl.2012.06.020.
Wessel, P., and W. H. F. Smith (1991), Free software helps map and display data, *EOS Trans. AGU*, *72*, 441.
Whitmeyer, S. J., and K. E. Karlstrom (2007), Tectonic model for the Proterozoic growth of North America, *Geosphere*, *3*(4), 220–259, doi:10.1130/ges00055.1.
Widess, M. (1973), How thin is a thin bed?, *Geophysics*, *38*, 1176–1180.
Williams, H., and R. D. Hatcher (1982), Suspect terranes and accretionary history of the Appalachian orogen, *Geology*, *10*(10), 530–536, doi:10.1130/0091-7613(1982)10 < 530:STAAHO > 2.0.CO;2.
Yuan, H. Y., K. Dueker, and D. L. Schutt (2008), Testing five of the simplest upper mantle anisotropic velocity parameterizations using teleseismic S and SKS data from the Billings, Montana PASSCAL array, *J. Geophys. Res.*, *113*, B03304, doi:10.1029/2007JB005092.
Yuan, H., and B. Romanowicz (2010), Lithospheric layering in the North American craton, *Nature*, *466*, 1063–1068.
Yuan, H., B. Romanowicz, K. M. Fischer, and D. Abt (2011), 3-D shear wave radially and azimuthally anisotropic velocity model of the North American upper mantle, *Geophys. J. Int.*, *184*, 1237–1260.
Yuan, H., S. French, P. Cupillard, and B. Romanowicz (2014), Geological units and their lithospheric expression in central and eastern north America from full waveform tomography, *Earth Planet. Sci. Lett.*, doi:10.1016/j.epsl.2013.11.057, in press.
Zhang, S., and S.-I. Karato (1995), Lattice preferred orientation of olivine aggregates deformed in simple shear, *Nature*, *375*, 774–777.